Manuscript Details

Manuscript number	COST_2018_3583
Title	Mechanical behavior of concrete prisms reinforced with steel and GFRP bar systems
Article type	Full Length Article

Abstract

Being immune to corrosion, and having a tensile strength up to three times higher than structural steel, glass fiber reinforced polymer (GFRP) bars are suitable for reinforcing concrete structures exposed to aggressive environmental conditions. However, a relatively low elasticity modulus of GFRP bars favors the occurrence of relatively large deformability of cracked reinforced concrete. Lack of ductility and degradation of properties under high temperature can be also identified as debilities of GFRP bars over steel ones. Combining GFRP and steel bars can be a suitable solution to overcoming these concerns. Nevertheless, the application of such reinforcement systems requires reliable material models. Unfortunately, the influence of the relative area of GFRP and steel bars on the tensile capacity of cracked concrete was never investigated from the experimental point of view, mainly crossing results from different tools on the assessment of the cracking process. This paper experimentally investigates deformations and cracking behavior of concrete prisms reinforced with different arrangements of steel and GFRP bars. The test results of 11 elements are reported. The cracking process is analyzed considering the hybrid reinforcement particularities and a preliminary approach is proposed for the prediction of the crack width for this type of reinforced concrete elements.

Keywords	B. Mechanical properties; B. Transverse cracking; C. Analytical modelling; D. Mechanical testing.

Corresponding Author	Viktor Gribniak
Corresponding Author's Institution	Vilnius Gediminas Technical University
Order of Authors	Arvydas Rimkus, Joaquim Barros, Viktor Gribniak, Mohammadali Rezazadeh
Suggested reviewers	Sami Rizkalla, Lawrence Bank, Brahim Benmokrane

Submission Files Included in this PDF

File Name [File Type]

Cover-letter CS.doc [Cover Letter]

Rimkus et al.docx [Manuscript File]

To view all the submission files, including those not included in the PDF, click on the manuscript title on your EVISE Homepage, then click 'Download zip file'.

Research Data Related to this Submission

There are no linked research data sets for this submission. The following reason is given:
No data was used for the research described in the article

The Editor-in-Chief
Composite Structures
Professor *Antonio Joaquim Mendes Ferreira*

Dear Sir,

Manuscript Title:
“Mechanical behavior of concrete prisms reinforced with steel and GFRP bar systems”

I hereby submit the above manuscript for consideration for possible publication in *Composite Structures*. It summarizes results of international cooperation of *Vilnius Gediminas Technical University* (*VGTU*, Lithuania) and *Minho University* (Portugal). An experimental study conducted at the *Laboratory of Innovative Building Structures*, *VGTU*. Being a part of the *Center for Physical Sciences and Technology of Lithuania*, the laboratory was recently renewed with state of the art equipment for material and structural tests.

Despite the apparent simplicity of the test setup, interpretation of tensile test results of reinforced concrete prisms is still a challenging task, mainly when is intended to derive reliable information for feeding the calibration of advanced numerical models and design guidelines on the tension stiffening, crack opening and crack spacing of concrete reinforced with hybrid systems. According to the knowledge of the present authors, the influence of the relative percentage of this hybrid reinforcement on the post-cracking tensile capacity of surrounding concrete (generally designated as tension stiffening effect) was never investigated from the experimental point of view.

The present study is dedicated to cracking and deformation analysis of concrete ties reinforced with steel and GFRP (glass fiber reinforced polymer) bar systems. Special equipment has been developed for testing ties reinforced with multiple bars. Due to extra challenges in terms of testing setup, its detailed description is provided. After the yield initiation of steel bars, elements with hybrid reinforcement demonstrate a pseudo-hardening stage. To represent this peculiar behavior, a conceptual tension stiffening model was proposed. This information is of paramount importance for simulating the contribution of concrete in tension in these circumstances when using a fibrous or layer approach, or a much more sophisticated numerical approach based on the finite element method. The cracking mechanism is analyzed considering the hybrid reinforcement particularities. A simple approach is proposed for estimating the average crack width at concrete surface from the average strain in the reinforcement.

Please contact me, if you require any further information. I look forward to receiving the reviewers’ comments and your decision.

Yours sincerely,

Viktor Gribniak
Ph.D., Chief Researcher,
Head of Laboratory of Innovative Building Structures,
Professor of Department of Steel and Composite Structures
Vilnius Gediminas Technical University,
Sauletekio av. 11, LT-10223 Vilnius, Lithuania
E-mail: Viktor.Gribniak@vgtu.lt

MECHANICAL BEHAVIOR OF CONCRETE PRISMS REINFORCED WITH STEEL AND GFRP BAR SYSTEMS

Arvydas Rimkus[1], Joaquim A. O. Barros[2], Viktor Gribniak[1*], Mohammadali Rezazadeh[2]

[1] Research Laboratory of Innovative Building Structures, Vilnius Gediminas Technical University, Sauletekio av. 11, 10223, Vilnius, Lithuania

[2] ISISE, Department of Civil Engineering, Minho University, Campus de Azurém, 4800-058 Guimarães, Portugal

[*] Corresponding author: **VIKTOR GRIBNIAK**, Vilnius Gediminas Technical University, Sauletekio av. 11, Vilnius LT-10223, Lithuania, E-mail: Viktor.Gribniak@vgtu.lt; Tel: +370 6 1346759

Abstract. Being immune to corrosion, and having a tensile strength up to three times higher than structural steel, glass fiber reinforced polymer (GFRP) bars are suitable for reinforcing concrete structures exposed to aggressive environmental conditions. However, a relatively low elasticity modulus of GFRP bars (in respect to the steel) favors the occurrence of relatively large deformability of cracked reinforced concrete. Lack of ductility and degradation of properties under high temperature can be also identified as debilities of GFRP bars over steel ones. Combining GFRP and steel bars can be a suitable solution to overcoming these concerns. Nevertheless, the application of such reinforcement systems requires reliable material models. Unfortunately, the influence of the relative area of GFRP and steel bars on the tensile capacity of cracked concrete (generally known as tension stiffening effect) was never investigated from the experimental point of view, mainly crossing results from different tools on the assessment of the cracking process. This paper experimentally investigates deformations and cracking behavior of concrete prisms reinforced with different arrangements of steel and GFRP bars. The test results of 11 elements are reported. Based on the experimental results a conceptual tension stiffening stress-strain relationship is proposed. The cracking process in terms of crack width and crack spacing is analyzed considering the hybrid reinforcement particularities and a preliminary approach is proposed for the prediction of the crack width for this type of reinforced concrete elements.

Keywords. B. Mechanical properties; B. Transverse cracking; C. Analytical modelling; D. Mechanical testing.

1. INTRODUCTION

Since the early 1980s, fiber reinforced polymers (FRP) are considered to be a promising alternative to steel reinforcement, especially in concrete structures subjected to aggressive environment or to the effects of electromagnetic fields [1]. Being immune to corrosion, and having a tensile strength up to 3 to 6 times higher than structural steel, FRP bars can be a suitable reinforcement for concrete structures, mainly those exposed to environmental aggressive conditions, like buildings and infrastructures in coastal and maritime zones. However, the low elastic modulus of some types of FRP materials (in respect to the steel), such is the case of glass fiber reinforced polymer (GFRP) bars, favors the occurrence of relatively large deformability in FRP reinforced concrete (RC) elements [2, 3]. Taking into consideration price and mechanical performance attributes of FRP reinforcements, GFRP bars are the most used in structural applications [4-6]. The higher deformability of concrete structures reinforced with GFRP bars is also caused by the smaller bond stiffness of these bars, when compared to the actual generation of steel bars used for the reinforcement of concrete structures [7-9]. This aspect promotes the occurrence of smaller number of cracks (larger crack spacing) of larger crack width at serviceability limit state (SLS) conditions, when steel reinforcement is considered for comparison purposes [10-12]. The larger crack width may not be a concern, considering the immunity of GFRP bars to corrosion. However, the tensile stress in the GFRP bars crossed by a crack increases significantly with the crack opening, which can be problematic in terms of premature local tensile rupture of these bars, mainly in structures submitted to fatigue loadings [13, 14]. If this type of failure occurs, the structural rupture can be catastrophic if no further ductile reinforcement is present to sustain the loss of capacity due to the failure. Furthermore, it is well known the debility of FRP bars to high temperatures [15-17]. Therefore, in case of a fire, the tensile capacity and bond conditions of FRP bars decrease significantly [18-21], compromising the structural safety of RC structures not properly designed for these circumstances.

Some attempts are being made to attenuate, or even overcome, the drawbacks pointed out to FRP reinforcements. One of the promising strategies is combining FRP and steel bars for the flexural reinforcement, by applying the FRP bars with the highest internal arm, i.e., with the minimum concrete cover thickness as possible, in order to take advantage of the relatively high tensile capacity of this reinforcement and its immunity to corrosion. For guaranteeing the required level of ductility, as well as the necessary safety in case of a fire, steel bars are also used with a sufficient concrete cover [22-24]. Such reinforcement layout also ensures protection from corrosion of the steel bars since the outer layer of the FRP reinforcement offers resistance to the development of macro cracks by promoting the formation of multiple secondary cracks. This FRP/steel reinforcement is regularly designated by hybrid reinforcement. Combining different materials in the same bar has also been explored in the context of hybrid reinforcement [25-28]. The cost competitiveness and reinforcement performance seem, however, lower than the previous concept of hybrid reinforcement, where bars of different type of materials are disposed in the concrete structure in order to mobilize, as much as possible, their potentialities [24, 29-32].

Mazaheripour et al. [8] has demonstrated that below a certain concrete cover thickness (15 mm), the bond of GFRP is detrimentally affected due to the formation of splitting tensile cracks in the alignment of the GFRP bars used for the flexural reinforcement. The susceptibility to the formation of this type of cracks should be dependent of the axial stiffness of the flexural reinforcement, by increasing with this stiffness. In this context, *Erki & Rizkalla* [33] and *Borosnyoi & Balazs* [34] stated that the minimum cover requirement for FRP systems should exceed the values specified for the steel reinforcement to avoid concrete cover splitting failures. The producers of GFRP bars [35, 36] recommend the two-diameter condition as a rational limitation for the minimum cover thickness.

For predicting the contribution of the tensile capacity of concrete surrounding the hybrid flexural reinforcement for the cracking behavior, a tension stiffening model was developed capable of estimating the crack width and crack spacing from the relevant properties of the intervening materials and assuming a bond low for FRP/steel versus surrounding concrete [37]. To validate the proposed model, reliable test data is essential. However, limited number of direct tensile tests of concrete elements reinforced with FRP and steel bars is available. The investigation by *Coccia et al.* [38] should be mentioned as an exceptional contribution in this concern, though a uniform deformational behavior for the GFRP and steel bars was not ensured in these tests. According to the knowledge of the present authors, the influence of the relative percentage of this hybrid reinforcement on the post-cracking tensile capacity of surrounding concrete (generally designated as tension stiffening effect) was never investigated from the experimental point of view; therefore, no reliable experimental results exist for this purpose. This information is of paramount importance for simulating the contribution of concrete in tension in these circumstances when using a fibrous or layer approach, or a much more sophisticated numerical approach based on the finite element method (FEM). In this last type of approaches, especially when using a smeared crack model, the post-cracking tensile capacity of concrete not influenced by reinforcement can be derived from the recommendations of *Model Code 2010* [39], based on the principles of fracture mechanics. However, for modeling the post-cracking tensile capacity of concrete under the influence of the bond mechanisms of the hybrid flexural reinforcement, the available information is quite scarce.

This paper experimentally investigates deformations and cracking behavior of concrete prisms reinforced with different arrangements of steel and GFRP bars. Due to extra challenges in terms of testing setup, its detailed description is provided. In an attempt of having reliable information of the cracking process for assisting in the interpretation of test results, digital image correlation (DIC) technique was also adopted, complementing an extensive monitoring system for measuring the deformation of the constituent materials. The experimental program is composed of eleven direct tensile tests, three of them exclusively reinforced with steel bars for serving as reference results, and the remaining eight ties are organized in four groups of two twins with different hybrid reinforcement configurations. Based on the experimental results, this work aims to evaluate the influence of relevant properties of the hybrid reinforcement on the tensile capacity of the surrounding concrete, crack opening and spacing, in order to contribute for the development of strategies for modeling the tension stiffening effect and cracking behavior of hybrid reinforced concrete structures.

2. EXPERIMENTAL RESEARCH

2.1. Test Program

The experimental program consists of eleven ties: eight with hybrid reinforcement (i.e. combination of steel and GFRP bars); and three reinforced exclusively with steel bars (reference). All ties had the same 150 × 150 mm cross-section and 500 mm length of the concrete part; the concrete cover was also constant and equal to 30 mm. All ties were reinforced with eight bars. The type of GFRP bars of 8 and 12 mm diameter, and steel bars of 6, 8 and 10 mm diameter, shown in Fig. 1, were used for the reinforcement. To determine the mechanical properties of the steel, three samples of each bar diameter were tested. The average stress-strain diagrams of the steel bars are presented in Fig. 2. The GFRP bars were not tested, since available information indicates the mechanical properties specified by the producer can be reliably used [40]. The corresponding mechanical properties are given in Table 1, which also includes the relevant properties obtained in the tensile tests of steel bars.

The adopted reinforcement configurations are presented in Fig. 3 and Table 2. Nomenclature of the ties characterizes the configuration of the reinforcement, including the number, material (the letter “*G*” defines GFRP, while “*S*” represents steel), and diameter of the bars. Nomenclature of the prisms with hybrid (steel + GFRP) reinforcement consists of two components separated by the slash symbol (“/”). Each of the hybrid reinforcement layouts is represented by two prisms (twin-specimens) numbered as “*1*” and “*2*”, e.g., *4G12/4S10-1* and *4G12/4S10-2* represent the first and second specimen, respectively, of the group reinforced with 4 GFRP bars of 12 mm diameter and 4 steel bars of 10 mm diameter. The experimental program also includes three reference prisms reinforced with eight steel bars of 10 mm diameter: one with a cross (X) shape distribution of the bars (*8S10X*), and two with a rectangular (R) arrangement of the bars (*8S10R-1*, *8S10R-2*).

For taking into consideration the existence of different materials in the hybrid reinforcement configurations, the concept of equivalent steel reinforcement ratio, $\rho_{s,eq}$, is used:

$$\rho_{s,eq} = \frac{1}{A_c} \cdot \left(A_s + A_f \cdot \frac{E_f}{E_s} \right), \qquad (1)$$

where the GFRP reinforcement is transformed in an equivalent steel reinforcement. In this equation A_c is the area of concrete section (150 × 150 mm minus the area occupied by the steel, A_s, and GFRP bars, A_f), A_s and A_f are the cross sectional area of the steel and GFRP reinforcement, respectively, and E_s and E_f are the modulus of elasticity of steel and GFRP reinforcement. The obtained values for $\rho_{s,eq}$ are indicated in Table 2. Varying from 0.8% to 2.1%, the $\rho_{s,eq}$, is within a so-called *rational* range of reinforcement ratio(0.4% to 3.5%) identified by *Gribniak et al.* [41] using test data of more than 300 RC ties. The latter range covers RC prisms representative for the analysis of the tension stiffening effect. In this table, the ratio between the axial stiffness of GFRP (A_fE_f) and steel reinforcements (A_sE_s), herein denominated as reinforcement stiffness ratio, is also included:

$$k_{f/s}^{a} = \frac{k_f^a}{k_s^a} = \frac{A_f E_f}{A_s E_s} \tag{2a}$$

in order to assess its influence on the behavior of the tested ties. It should be realized that this concept is the same of the following one:

$$\frac{\rho_{f\rightarrow s}}{\rho_s} = \frac{A_f}{A_s} \cdot \frac{E_f}{E_s}, \tag{2b}$$

where the GFRP reinforcement ratio, transformed in an equivalent steel reinforcement ratio ($\rho_{f\rightarrow s}$ = [$A_f \cdot E_f$ / E_s] / A_c) is divided by the steel reinforcement ratio (ρ_s = A_s / A_c).

Gribniak & Rimkus [42] developed a specific anchorage blocks for fixing the multiple bars, as part of the test setup shown in Fig. 4. Each anchorage block is connected to the tension equipment using a spherical hinge (Fig. 4) that allows avoiding a possible imperfection in applying the tensile load (related to an inhomogeneity of the concrete tie and non-uniform development of the cracks). Steel clamps are used for an additional confinement of the bars within the anchorage blocks.

The specimens were produced using similar site-mix concrete with maximum aggregate size of 8 mm and compressive strength class C30/37. All samples (including 12 cylinder specimens) were stored into water to reduce the shrinkage effect. The ties were tested at 9, 10 and 11 days after have been cast. The results of the compressive ∅150 × 300 mm cylinder tests are presented in Table 3. As can be observed, the average compressive strength of the concrete interpolated at the tie test day was equal to 42.4 MPa, which indicates that the adopted concrete can be considered of strength class C35/40 at testing age (the characteristic value of cylinder compressive strength is about 35 MPa).

The tensile tests were performed using a servo-hydraulic testing machine of 600 kN capacity in displacement control at the rate of 0.2 mm/min. The load was monitored by the electronic load cells of the testing equipment. The axial deformations were measured using linear variable displacement transducers (LVDT) that were attached to the reinforcement bars and to the concrete surface, as shown in Fig. 4.

2.2. Test Results and Discussion

2.2.1. Deformations

The determined load versus average strain diagrams are shown in Fig. 5, while the respective average normalized stress versus average normalized strain relations are illustrated in Fig. 6. The average strains (abscissa) were divided by the theoretical cracking strain, $\varepsilon_{cr} = f_{ctm} / E_{cm}$, where the average tensile strength f_{ctm} and the modulus of elasticity E_{cm} of concrete were determined by the recommendations of *Model Code 2010* [39] using respective values of the compressive strength f_{cm} at testing age (from Table 3). The secondary abscissa (shown at the top of the diagram) shows the actual strain scale. The ordinate represents the tensile stress σ_{ct} divided by the f_{ctm}. The diagrams shown in Figs. 6a and 6b were determined using the average deformations of the reinforcement and of the concrete surface, respectively.

The concrete tensile stress-strain diagrams presented in Fig. 6a (whose post-cracking stage represents the tension-stiffening effect) were determined using the average strain measured in the reinforcement bars (ε_r):

$$\sigma_{c,r} = \frac{\mathbf{P} - \mathbf{N}_{r,r}}{A_c} = \frac{\mathbf{P} - \varepsilon_r \cdot (A_f E_f + A_s E_s)}{A_t - (A_f + A_s)}; \quad \varepsilon_r E_t \leq f_y, \tag{3a}$$

where A_t is the cross section of the tie (150 × 150 mm); **P** is the applied tensile load; $\mathbf{N}_{r,r}$ is the force supported by the reinforcement, determined from the strains measured in the reinforcement; ε_r is the average strain of the reinforcement bars; f_y is the yielding stress of the steel reinforcement. In the hybrid specimens the ε_r was in fact evaluated from the average deformation recorded in the GFRP bars (Fig. 4), having been assumed that steel bars presented equal average strain, which seems a realistic assumption due to the test setup adopted.

The stress-strain diagrams presented in Fig. 6b were determined using the average deformations of the concrete surface:

$$\sigma_{c,c} = \frac{\mathbf{P} - \mathbf{N}_{r,c}}{A_c} = \frac{\mathbf{P} - \varepsilon_c \cdot (A_f E_f + A_s E_s)}{A_t - (A_f + A_s)}; \quad \varepsilon_c E_t \leq f_y, \tag{3b}$$

where $\mathbf{N}_{r,c}$ is the force supported by the reinforcement determined from the average strain measured on the concrete surface, ε_c. It can be observed that the stress-strain diagrams determined using the average strains of reinforcement bars and concrete surface are different. The differences can be attributed to the non-uniform distribution of tensile strains within the concrete. A more detail discussion of this issue can be found in the study conducted by *Rimkus* [43].

Figs. 5 and 6 indicate that the hybrid combination of reinforcement is quite efficient allowing to exploit the steel reinforcement within the post-yielding stage. The diagrams of Fig. 5a and 6a show a hardening stage of the specimens after the yielding of the steel bars. If steel was the unique reinforcement, the load carrying capacity of the tie will be almost coincident with the yield initiation of the steel reinforcement. Stiffness of the ties with hybrid reinforcement, however, starts decreasing after the yield initiation of steel bars. This decrease has the tendency of being the higher the smaller is $k_{f/s}$ (the axial stiffness of GFRP reinforcement decreases regarding the axial stiffness of steel reinforcement). This is not visible in the *4G12/4S10* ties because the tests of these ties were interrupted at yield initiation of the steel bars. The reported tendency can also be inferred by adding the theoretical “bare bar” response Fig. 5a, which was done by adopting the material properties presented in Table 1.

The tests of the *4G8/4S6-1* and *4G8/4S6-2* specimens (reinforced with 8 mm GFRP and 6 mm steel bars) were terminated after rupture of the steel bars within the uncovered part of the specimens (Fig. 7), but these ties did not fail completely since the GFRP bars were capable to resist the tensile load. To avoid the brittle failure of the GFRP bars, these specimens were tested until the tensile deformations approached the theoretical ultimate strain of these bars (Table 1).

Differences of the tensile stress-strain diagrams of Fig. 6a are due to different origins. The following comments can be made in this regard:

- For ε_r / ε_{cr} above of approximately 20, the specimens *4G8/4S8* (with the lowest $k\,{}^{a}\!/_{f/s}$ ratio) presented a negative concrete post-cracking tensile capacity $\sigma_{c,r}$ / f_{ct} < 0. The relatively low axial stiffness of GFRP bars maybe not capable of uptaking the stresses transferred from reinforcement to surrounding concrete after yield initiation of steel bars. The "negative" tension stiffening effect obtained by using Eq. (3a) may also be justified by the assumed equal average strain for the steel and GFRP bars ($\varepsilon_r = \varepsilon_s = \varepsilon_f$). As already indicated, the ε_r was obtained by measuring exclusively the strains in the GFRP bars; therefore, $\varepsilon_r = \varepsilon_f$. However, if strains in the steel bars are less than the strains measured in the GFRP bars the negative concrete tensile capacity can be eliminated. This can also happen in case the real E_f value be smaller than the one provided by the supplier.
- In combination with a relatively low $k\,{}^{a}\!/_{f/s}$ ratio, high relative equivalent reinforcement ratio ($\rho_{s,eq}$) in the ties *4G12/4S10* has contributed for these ties

have had similar behavior to the one of the reference specimens (reinforced with steel bars).

- Reinforcement layout of the ties *4G12/4S6* seems to be the most effective amongst the considered samples in terms of providing the highest concrete post-cracking tensile capacity.

Adequate assessment of the tension stiffening effect is one of the most challenging issues for adequate modelling of RC members, mainly for serviceability limit state (SLS) conditions, due to its influence on the stiffness evolution of cracked concrete [44]. Bond of the reinforcement to the surrounding concrete is also a property of relevant influence of the performance of RC structures at SLS. Deficient bond demonstrated by some FRP reinforcements, amplifies the difference between ε_c and ε_r, due to relatively large sliding between these reinforcements and surrounding concrete, being more arguable the use of ε_c for the evaluation of the tension stiffening diagrams.

Based on the results presented in Fig. 5a and 6a, the physical representation of the tensile stress-strain diagram for ties with hybrid reinforcement is illustrated in Fig. 8, where the post cracking tensile capacity of concrete represents the tension-stiffening effect. For assisting on the justification of the influence of the cracking process on the tension stiffening diagrams, two representative specimens were selected, and this information is represented in Fig. 9. The diagrams of Fig. 9 are characterized by the following stages (represented in Fig. 8 for generalization of the concepts): 0A – linear elastic stage, where A corresponds to the load $\mathbf{P}_{el}$ and the strain ε_{el} when microcracks are formed; AE – crack formation stage; EG – stabilized cracking stage. The stage AE can be decomposed on the following sub-stages: AB – the stiffness of the tie decreases due to the micro-cracking propagation (Fig. 8a), but the tensile capacity of concrete is still increasing (Figs. 8b and 9). At the end of this sub-stage, the load and corresponding strain are represented by $\mathbf{P}_{cr}$ and ε_{cr}, respectively, and the first crack becomes visible (Fig. 9, in this AB sub-stage the micro-cracks were not visible); BC – intense propagation of cracks with an abrupt decay of the tensile capacity of concrete, while the load was maintained almost constant (the stages AB and BC are mainly governed by the fracture energy of the concrete, G_f); CD – the load carrying capacity increases up to an average strain in the reinforcement equal to the yield strain of the steel bars (load $\mathbf{P}_{sy}$ and corresponding strain ε_{sy}). Note that when $\varepsilon_r = \varepsilon_{sy}$ (point D) the steel reinforcement has already yielded at a cracked section level. The stress decay during this stage is as higher as smaller is kf^{q}_{s} and p_f / p_s, see Table 2 and Fig. 8a, which can be justified by the better bond properties of steel bars compared to the GFRP bars and relative bond perimeter between these reinforcements. In these circumstances, the end of the cracking stabilization process tends to occur for average strain levels in the reinforcement higher than the yield initiation of the steel reinforcement, $\varepsilon_r > \varepsilon_{sy}$, (E point stays in the DF stage). This is illustrated in the cracking process of *4G8/4S6-2* represented in Fig. 9b, where the last visible crack has been formed after yield initiation. The cracking process of *4G12/4S10-1* represented in Fig. 9a demonstrates that all cracks were formed before yield initiation due to relatively high $\rho_{s,eq}$ and low kf^{q}_{s}. After yield initiation (represented by point D), a pseudo-hardening stage (Figs. 6a, 8b and 9b) can be formed, and is as pronounced as smaller is $\rho_{s,eq}$ and higher is kf^{q}_{s} and p_f / p_s, due to the reasons already exposed, which was also demonstrated by

Mazaheripour *et al.* [37]. In these circumstances, the crack stabilization process coincides with the peak stress that occurs after the yield initiation of the steel bars (represented by point F in Fig. 8). After the stabilized cracking stage, and steel reinforcement already yielded, the response is mainly governed by the stiffness of the GFRP reinforcement, and the cracks already formed are opening, with a smooth decrease of the concrete post-cracking tensile capacity (Figs. 6a, 8b and 9b), which is a consequence of the bond damage propagation.

In resume, and according to the main evidences from the analytical model of Mazaheripour *et al.* [37], the experimental results obtained in the tests carried out demonstrated that in the relevant stages of the post-cracking process, the concrete tensile capacity increases with $k_{f/s}^{a}$ and p_f / p_s.

2.2.2. Cracking

The final crack pattern of the ties with hybrid reinforcement is shown in Fig. 10. As it can be observed, the shape of the crack patterns is not regular in most cases. Moreover, the final patterns are related with different ultimate strains of reinforcement, $\varepsilon_{r,ult}$.

To compare crack evolution, the DIC system was used. In Fig. 10, the surface exposed for the image correlation procedure (surface “1”) is designated as (DIC). The digital images were captured using two digital cameras *Imager E-lite 5M*. The cameras, incorporating a charge-coupled device (CCD) detector, have a resolution of 2456×2085 pixel at 12.2 fps rate. The cameras were placed vertically on a tripod at 2.5 m distance from the test specimens. The use of two cameras enabled reliable capturing of image data within their respective focal zone to minimize errors due to aberration. The *DaVis 8.1.6* software by *La vision* was used for tracing relative displacements of the surface points. Fig. 11 presents an example of the evolution of the cracks identified by the DIC system in the *4G8/4S8-2* specimen. The cracking development tendencies are evident from the captured digital views (the vertical white strip at the specimen center corresponds to the shadow of the bar supporting the LVDT, as shown in Fig. 4).

Fig. 12 presents series of the cracking patterns identified by the DIC system. The patterns identified for all considered specimens are related to the same average strain of the reinforcement, ε_r. This figure also includes results of the reference prisms (*8S10X* and 8*S10R-1/2*) reinforced with steel bars only. The reference specimens demonstrate a different cracking character than those observed on the prisms with hybrid reinforcement. The differences are evident in the earliest loading stages (ε_r = 0.05% to 0.10%), when multiple cracks have been formed in the reference specimens, while smaller number of cracks was registered in the hybrid reinforced specimens for this stage. The decrease of the number of cracks is accentuated with the decrease of $\rho_{s,eq}$, due to the smaller load level applied to the tie.

A quasi-stabilized crack pattern is attained at an average strain in the reinforcement in the interval of 0.20% to 0.25% (ε_r = 0.002–0.0025), which is in agreement with the interpretation provided in Fig. 8. To deep analyze the cracking process, crack width tendencies were also investigated. As Mazaheripour *et al.* [37] demonstrated, the average crack width, $\overline{w}_{cr}$, and the average strain of element, $\varepsilon_{r/c}$, could be related as following:

$$\varepsilon_{r/c} = \frac{\overline{w}_{cr}}{\overline{L}_{cr}} + \overline{\varepsilon}_{cr}, \tag{4a}$$

where the average crack spacing, $\overline{L}_{cr}$, and the average crack width, $\overline{w}_{cr}$, are determined as

$$\overline{L}_{cr} = \frac{\sum_{i=1}^{n_{cr}} L_{cr,i}}{n_{cr}} \tag{4b}$$

and

$$\overline{w}_{cr} = \frac{1}{n_{cr}} \sum_{i=1}^{n_{cr}} w_{cr,i}. \tag{4c}$$

In the above equations, n_{cr} is the number of cracks formed in the concrete prism; $w_{cr,i}$ and $L_{cr,i}$ are the crack width and crack spacing of the i^{th} crack; $\overline{\varepsilon}_{cr}$ is the average strain of element at concrete cracking initiation. However, as it was shown in the previous section, significant differences were registered in the average strains recorded on the reinforcement and on the concrete surface. To investigate adequacy of Eq. (4a), the crack widths registered experimentally were also considered for this analysis.

At selected loading levels, the crack width was measured using digital microscope *CK102* with 40× magnification as shown in Fig. 13. The cracks were measured at the surface exposed to the DIC system. The measurement points were at the intersection of the crack with the GFRP bars, as illustrated in Fig. 10. In this figure, the dashed lines indicate the position of the GFRP bars, while the dots correspond to the measurement position. The dot numbers indicate the cracking sequence; the letters “L” (“left”) and “R” (“right”) correspond to the monitoring line.

Fig. 14 presents the relationship between crack width (averaging “L” and “R” measurements for each crack, Fig. 10) and average strain in the reinforcement. Stochastic development of the internal cracks might be responsible for the evident differences in the number of visible cracks (Fig. 12): no pair of nominally identical twin-specimens demonstrates the same number of cracks. Averaging procedure, however, remedies the cracking results. As can be observed in Fig. 14, the average crack width is very similar in all hybrid specimens though the number of cracks varies significantly.

Fig. 15 shows the relationship between equivalent steel reinforcement ratio, $\rho_{s,eq}$, and average crack width obtained using optical microscope. It can be observed that the ties with higher equivalent reinforcement ratio ($\rho_{s,eq}$ = 2.1%) maintains practically constant crack width (independently on the reinforcement strain, ε_r). By decreasing $\rho_{s,eq}$, the crack width becomes more sensitive to the strain level applied to the reinforcement. Furthermore, cracks in these elements were only visible at higher deformation levels (Fig. 12).

The rate $\overline{w}_{cr}$ / ε_r has also a tendency to increase with the coefficient $k^{a}_{f/s}$ and the ratio p_f / p_s due to the lowest bond performance of GFRP bars over steel bars, as already indicated. In fact, for the series of largest $k^{a}_{f/s}$ and p_f / p_s (*4G12/4S6*) a value of about

0.065 mm/‰ was obtained, while in the series of smallest values for these variables (*4G8/4S8*) a value of about 0.056 mm/‰ was determined.

Width of the cracks was also estimated using the DIC system. Fig. 16 shows the distribution of the relative displacements of the surface of the *4G12/S46-1* specimen corresponding to the average strain of the reinforcement ε_r = 0.42%. The relative displacement distribution profile in the alignment of a GFRP bar (referred in Fig. 16 by **S-S** section) was obtained using digital images of the concrete surface. For this purpose, the position of each point on the surface is identified by applying a particular correlation algorithm (*DaVis 8.1.6* software by *La vision*) to the same points from reference image. Knowledge of the precise position of every point at every loading step allows tracking the surface movement for obtaining the distribution map of the strains. Displacement profile is collected from points on the surface at intervals of 0.3 mm along the **S-S** section. The peak displacements correspond to the locations of the actual cracks. The area beneath the identified surface strain diagram represents the accumulative displacement of the concrete surface. The area above the theoretical cracking strain ε_{cr} (Fig. 16) is equivalent of the cumulative crack opening deformations. Following this concept, the average crack width can be determined by applying the following equations:

$$\overline{w}_{cr} = \frac{\int_0^L \varepsilon_c^* dl}{L} \cdot \overline{L}_{cr} \cdot k_w, \quad (5a)$$

where the corresponding positive strain, ε_c^*, obtained by shifting the abscissa to the theoretical cracking strain point, ε_{cr}, is expressed as

$$\varepsilon_c^* = \begin{cases} \varepsilon_c - \varepsilon_{cr}, & \varepsilon_c > \varepsilon_{cr} \\ 0, & \varepsilon_c \le \varepsilon_{cr} \end{cases}, \tag{5b}$$

while the profile shape coefficient k_w is determined as the ratio between the cumulative length of the segments corresponding positive values of the strain ε_c^* to the total length of the concrete prism L:

$$k_w = \frac{1}{L}\sum_i L_{w,i}. \tag{5c}$$

In above equations, the average crack distance $\overline{L}_{cr}$ is obtained from Eq. (4b).

Table 4 summarizes the cracking results. In this table, the average crack distance $\overline{L}_{cr}$ is determined considering cracks captured by using the DIC system in the surface of the concrete prism exposed for the image correlation procedure. This surface is designated as (DIC) in Fig. 10. The crack patterns presented in Fig. 12 demonstrates the diverse behavior (length) of the external and internal concrete blocks formed, respectively, between the transverse cracks and at extremities of the prisms. Thus, the average crack distance assessed by averaging the lengths of all uncracked segments was assumed inadequate. Therefore, the average crack distance $\overline{L}_{cr}$ is determined excluding external uncracked blocks of the concrete. The crack widths are related with average deformations of both, bar reinforcement, ε_r, and concrete surface, ε_c. Results extracted from DIC data are based on selective relative strain ($\varepsilon_c > \varepsilon_{cr}$) associated with crack locations and their widths as described above. In some cases, however, the number of cracks measured with the microscope has not corresponded to the number of cracks observed using DIC technique (these results are shown at bold in the respective column). In these cases, experimental values obtained using DIC technique were assumed more reliable and adopted for the analysis. In some cases, significant noise of digital images has not allowed a precise identification of the cracking results by using the DIC system. The corresponding crack values are in between square brackets. These results should be considered as not reliable. From results presented in Table 4, the following conclusions can be pointed out:

1. Evaluating the average crack width ($\overline{w}_{cr}$) from Eq. (4c) by using for the corresponding average strain the value registered in the reinforcement ($\varepsilon_{r/c} = \varepsilon_r$) provides in general higher values than when adopted the average concrete strain ($\varepsilon_{r/c} = \varepsilon_c$) because, as already shown in Fig. 5, ε_r>ε_c.
2. The $\overline{w}_{cr}$ values obtained from Eq. (4c) by using $\varepsilon_{r/c} = \varepsilon_c$ are closer to the ones obtained with the microscope and DIC because all these approaches are based on records executed at concrete surface.
3. Crack width based on DIC is generally smaller than by microscope, mainly at larger deformation levels.

To improve the theoretical predictions based on application of Eq. (4a), a modification is suggested based on the physical interpretation of the Fig. 17 that shows the relationship between $\varepsilon_c/\varepsilon_r$ and ε_r in the tested specimens. All the specimens present similar response, with a pronounced decrease of the $\varepsilon_c/\varepsilon_r$ with the increase of ε_r up to a ε_r value in the interval of 0.02% and 0.07% corresponding to the strain range where cracks become visible in the surface of the specimens (see also Figs. 5a, 9 and 12). This limit corresponds to the point B in Fig. 8. In this stage, the load applied to the reinforcement has mainly induced strain increment in the reinforcement with relative small variation of strains in the concrete surface during the load transference process from the reinforcement to the surrounding concrete. Above this strain level in the reinforcement, the $\varepsilon_c/\varepsilon_r$ has increased with ε_r, but this increase has tended to a $\varepsilon_c/\varepsilon_r$ value of approximately 0.7. In this phase, the increase of $\varepsilon_c/\varepsilon_r$ with ε_r was initially quite pronounced, which corresponds to the first phase of the crack propagation stage, defined by the branch BC in Fig. 8. With the formation of more cracks up to the cracking stabilized stage the increase of $\varepsilon_c/\varepsilon_r$ with ε_r has continuously become less pronounced up to attain the above indicated limit. Two specimens have, however, not tended to this limit value of $\varepsilon_c/\varepsilon_r$, namely *4G8/4S6-2* and *4G12/4S6-2* (designated in Figs. 5b, 6b, and 17), which can be justified by the following reasons. The failure of the *4G8/4S6-2* prism was localized outside the monitoring zone (Fig. 7), which conducted to a lower bound envelope of the $\varepsilon_c/\varepsilon_r$-$\varepsilon_r$ relationship; in the opposite, the upper bound envelope of the $\varepsilon_c/\varepsilon_r$-$\varepsilon_r$ relationship registered in the *4G12/4S6-2* prism might be related with a possible measurement error.

This tendency enables to formulate the following improvement of the crack prediction model based on Eq. (4a):

$$\overline{w}_{cr} = \alpha_\varepsilon(\varepsilon_r - \overline{\varepsilon}_{cr})\overline{L}_{cr}, \tag{6}$$

where α_ε is a reduction coefficient that allows to estimate the average crack width at concrete surface from the average strain in the reinforcement. At yield initiation of the steel reinforcement $\alpha_\varepsilon \approx 0.65$. This value is well agreeing with the numerical simulation results of concrete prisms reinforced with multiple bars reported in the reference [45].

The corresponding results (modified crack widths) are presented in brackets in Table 4. It is important to note, however, that the suggested value of the coefficient α_ε is adequate for the particular loading scheme and geometry of the specimens. Identification of this coefficient values in different loading conditions and reinforcement schemes should be the object of further research.

The negative portion of the relative deformations determined in Fig. 17 could be attributed to a “negative” deformation of the concrete surface at the loads approaching the cracking moment. This effect could be also observed in Figs. 5b and 6b. In this regard, it should be recalled that the concrete prisms were loaded by applying tension load to the reinforcement bars (Fig. 4). Such loading scheme causes deformation localization in the concrete prism when transferring the bond stresses from the reinforcement to the surrounding concrete [43].

It is also worth to mention that, in concrete reinforced with steel bars, the previous indicated relationship is only valid up to yield initiation, due to the cracking localization in the yielded section. In specimens with hybrid reinforcement, the relationship between w_{max} and $\overline{w}_{cr}$ will increase after yield initiation, but due to the linear elastic stage of FRP reinforcement, the increase of this ratio should be much smaller than in conventional reinforced concrete. Fig. 18 shows that, in fact, after yield initiation, the average and maximal crack width ratio $\overline{w}_{cr}$ / w_{max} (obtained using the optical microscope) has varied in a relative small interval, between 0.65 and 0.8 up to the end of the tests.

3. CONCLUSIONS

Glass fiber reinforced polymer (GFRP) bars as structural reinforcement are suitable for application in concrete subjected to aggressive environmental conditions. However, limitations of mechanical properties, such as the low elasticity modulus, ductile failure, and debility to high temperatures, are becoming essential for development of engineering projects. Combined application of steel and GFRP bars can be considered as a prominent way for improving the structural performance at both serviceability and ultimate limit state conditions. The GFRP/steel reinforcement is regularly designated by hybrid reinforcement. Unfortunately, the influence of the relative area of GFRP and steel bars on tensile capacity of the cracked concrete (generally known as tension stiffening effect) was never investigated from the experimental point of view.

This paper experimentally investigates deformations and cracking behavior of concrete prisms reinforced with different arrangements of steel and GFRP bars. The conclusions are based on the tensile test results of 11 ties: eight with hybrid reinforcement (i.e. combination of steel and GFRP bars); and two reinforced exclusively with steel bars (reference). All ties had the same 150 × 150 mm cross-section and 500 mm length of the concrete part; the concrete cover was also constant and equal to 30 mm. All ties were reinforced with eight bars, of 8 and 12 mm diameter for the GFRP bars, and 6, 8 and 10 mm diameter for the steel bars. The area ratio of GFRP-to-steel varied from one to two. Based on the obtained results, the following conclusions can be pointed out:

1. The developed anchorage system is applicable for performing tension tests of concrete prisms reinforced with hybrid reinforcement systems. The proposed layout of monitoring devices enables identifying average deformations of both, bar reinforcement and concrete surface. The digital image correlation system is applicable for determining the crack width at concrete surface. The obtained information is useful for estimating strain distribution and crack formation in the concrete.
2. The average deformations of the reinforcement and of the concrete surface was found different. The difference can reach tenth times at the pre-cracking stage. It decreases with the increase of the reinforcement deformation.
3. After the yield initiation, elements with hybrid reinforcement demonstrate a pseudo-hardening stage. The “hardening” effect increases with the relative area of GFRP reinforcement and overall decrease of the reinforcement ratio. Arrangement of the hybrid reinforcement with the minimum total reinforcement ratio and relatively increased area proportion of GFRP bars provided the highest concrete post-cracking tensile capacity. To represent this specific behavior, a conceptual tension stiffening model was proposed. This information is of paramount importance for simulating the contribution of concrete in tension in these circumstances when using a fibrous or layer approach, or a much more sophisticated numerical approach based on the finite element method.
4. The cracking process in terms of crack width and crack spacing is analyzed considering the hybrid reinforcement particularities. Stochastic formation was

found responsible for the observed differences in the crack patterns: no pair of nominally identical twin-specimens demonstrates the same number of cracks. Averaging procedure, however, remedies the cracking results. By decreasing the reinforcement ratio of the hybrid reinforcement system the crack width becomes more sensitive to the strain level applied to the reinforcement. The variation of the average crack width with the applied average strain in the reinforcement had a tendency to increase with the relative axial stiffness and relative bond contact of the hybrid reinforcement due to the lowest bond performance of GFRP bars over steel bars. The average and maximal crack width ratio has varied in a relative small interval, between 0.65 and 0.8 up to the end of the tests.

5. A simple approach is proposed for estimating the average crack width at concrete surface from the average strain in the reinforcement. However, further investigation must be conducted in this regards in order to verify the eventual dependency of this approach on non-considered parameters like reinforcement configurations, concrete cover thickness, concrete strength class, and loading conditions.

ACKNOWLEDGEMENTS

The authors wish to express their sincere gratitude to the financial support by the Research Council of Lithuania (Research Project S-MIP-17-62). The second author also wish to acknowledge the support provided by FCT through the PTDC/ECM-EST/1882/2014 project.

REFERENCES

1. Torres L, Neocleous K, Pilakoutas K. Design procedure and simplified equations for the flexural capacity of concrete members reinforced with fibre-reinforced polymer bars. Structural Concrete 2012;13(2):119-129.

2. Mias C, Torres L, Turon A, Barris C. Experimental study of immediate and time-dependent deflections of GFRP reinforced concrete beams. Composite Structures 2013;96:279-285.

3. Mahmoud K, El-Salakawy E. Shear strength of GFRP-reinforced concrete continuous beams with minimum transverse reinforcement. ASCE Journal of Composites for Construction 2014;18(1), Paper ID: 04013018, 11 p.

4. Berg AC, Bank LC, Oliva MG, Russel JS. Construction and cost analysis of an FRP reinforced concrete bridge deck. Construction and Building Materials 2006;20(8):515-526.

5. Bouguerra K, Ahmed EA, El-Gamal S, Benmokrane B. Testing of full-scale concrete bridge deck slabs reinforced with fiber-reinforced polymer (FRP) bars. Construction and Building Materials 2011;25(10):3956-3965.

6. Zaman A, Gutub SA, Wafa MA. A review on FRP composites applications and durability concerns in the construction sector. Journal of Reinforced Plastics and Composites 2013;32(24):1966-1988.

7. Soong WH, Raghavan J, Rizkalla SH. Fundamental mechanisms of bonding of glass fiber reinforced polymer reinforcement to concrete. Construction and Building Materials 2011;25(6):2813-2821.

8. Mazaheripour H, Barros JAO, Sena-Cruz JM, Pepe M, Martinelli E. Experimental study on bond performance of GFRP bars in self-compacting steel fiber reinforced concrete. Composite Structures 2013;95:202-212.

9. Gudonis E, Kacianauskas R, Gribniak V, Weber A, Jakubovskis R, Kaklauskas G. Mechanical properties of the bond between GFRP reinforcing bars and concrete. Mechanics of Composite Materials 2014;50(4):457-466.

10. Saikia B, Kumar P, Thomas J, Rao KSN, Ramaswamy A. Strength and serviceability performance of beams reinforced with GFRP bars in flexure. Construction and Building Materials 2007;21(8):1709-1719.

11. Mazaheripour H, Barros JAO, Soltanzadeh F, Gonçalves DMF. Interfacial bond behaviour of GFRP bar in self-compacting fiber reinforced concrete. In: Proceedings of 8th RILEM International Symposium on Fibre Reinforced Concrete: Challenges and Opportunities. 2012, Guimaraes, Portugal, September 2012. p. 512-525.

12. Gribniak V, Caldentey AP, Kaklauskas G, Rimkus A, Sokolov A. Effect of arrangement of tensile reinforcement on flexural stiffness and cracking. Engineering Structures 2016;124:418-428.

13. Noël M, Soudki K. Fatigue behavior of GFRP reinforcing bars in air and in concrete. ASCE Journal of Composites for Construction 2014;18(5), Paper ID: 04014006, 8 p.

14. Noël M, Soudki K. Fatigue behavior of full-scale slab bridge strips with FRP reinforcement. ASCE Journal of Composites for Construction 2015:19(2), Paper ID: 04014047, 9 p.

15. Wang YC, Kodur V. Variation of strength and stiffness of fibre reinforced polymer reinforcing bars with temperature. Cement and Concrete Composites 2005;27(9-10):864-874.

16. Wang YC, Wong PMH, Kodur V. An experimental study of the mechanical properties of fibre reinforced polymer (FRP) and steel reinforcing bars at elevated temperatures. Composite Structures 2007;80(1):131-140.

17. Ou Y, Zhu D, Zhang H, Huang L, Yao Y, Li G, Mobasher B. Mechanical characterization of the tensile properties of glass fiber and its reinforced polymer (GFRP) composite under varying strain rates and temperatures. Polymers 2016;8(5), Paper ID: 196, 16 p.

18. Katz A, Berman N, Bank LC. Effect of high temperature on bond strength of FRP rebars. ASCE Journal of Composites for Construction 1999;3(2):73-81.

19. Saafi M. Effect of fire on FRP reinforced concrete members. Composite Structures 2002;58(1):10-20.

20. Bisby LA, Kodur VKR. Evaluating the fire endurance of concrete slabs reinforced with FRP bars: Considerations for a holistic approach. Composites Part B: Engineering 2007;38(5-6):547-558.

21. Hamad RJA, Johari MAM, Haddad RH. Mechanical properties and bond characteristics of different fiber reinforced polymer rebars at elevated temperatures. Construction and Building Materials 2017;142:521-535.

22. Leung HY, Balendran RV. Flexural behaviour of concrete beams internally reinforced with GFRP rods and steel rebars. Structural Survey 2003;21(4):146-157.

23. Liu Y, Yuan Y. Experimental studies on high strength concrete beams reinforced with steel and GFRP rebars. Applied Mechanics and Materials 2012;238:669-673.

24. Mazaheripour H, Barros JAO, Soltanzadeh F, Sena-Cruz JM. Deflection and cracking behavior of SFRSCC beams reinforced with hybrid prestressed GFRP and steel reinforcements. Engineering Structures 2016;125:546-565.

25. Henneke MJ. Evaluation of Hybrid Reinforcement (Fiber-Reinforced-Plastic Rod with Steel Core). MSc Thesis. The Pennsylvania State University, 1993. 158 p.

26. Harris H, Somboonsong W, Ko F. New ductile hybrid FRP reinforcing bar for concrete structures. ASCE Journal of Composites for Construction 1998;2(1):28-37.

27. Sun ZY, Yang Y, Qin WH, Ren ST, Wu G. Experimental study on flexural behavior of concrete beams reinforced by steel-fiber reinforced polymer composite bars. Journal of Reinforced Plastics and Composites 2012;31(24):1737-1745.

28. Park C, Park Y, Kim S, Ju M. New emerging surface treatment of hybrid GFRP bar for stronger durability of concrete structures. Smart Structures and Systems 2016;17(4):593-610.

29. Qu W, Zhang X, Huang H. Flexural behavior of concrete beams reinforced with hybrid (GFRP and steel) bars. ASCE Journal of Composites for Construction 2009;13(5):350-359.

30. Safan MA. Flexural behavior and design of steel-GFRP reinforced concrete beams. ACI Materials Journal 2013;110(6):677-686.

31. Ge W, Zhang J, Cao D, Tu Y. Flexural behaviors of hybrid concrete beams reinforced with BFRP bars and steel bars. Construction and Building Materials 2015;87:28-37.

32. Bencardino F, Condello A, Ombres L. Numerical and analytical modeling of concrete beams with steel, FRP and hybrid FRP-steel reinforcements. Composite Structures 2016;140:53-65.

33. Erki MA, Rizkalla SH. FRP reinforcement for concrete structures. Concrete International 1993;15(6):48-53.

34. Borosnyoi A, Balazs GL. Experiences and design considerations of concrete members reinforced with FRP. In: Proceedings of the International Seminar: Composite Materials in Concrete Construction. University of Dundee, Scotland, 2002. p. 135-146.

35. Hughes Brothers. Glass Fiber Reinforced Polymer (GFRP) Rebar – Aslan 100 Series. Seward: Hughes Brothers Inc., 2011. 16 p.

36. Fiberline Composites. ComFAR by Fiberline. Technical Documentation. Middelfart: Fiberline Composites S/A, 2017. 28 p.

37. Mazaheripour H, Barros JAO, Sena-Cruz S. Tension-stiffening model for FRC reinforced by hybrid FRP and steel bars. Composites Part B: Engineering 2016;88:162-181.

38. Coccia S, Meda A, Rinaldi Z, Spagnuolo S. Influence of GFRP skin reinforcement on the crack evolution in RC ties. Composites Part B: Engineering 2017;119:90-100.

39. *fib* (International Federation for Structural Concrete). Model Code for Concrete Structures 2010. Berlin: Wilhelm Ernst & Sohn, 2013. 434 p.

40. Schöck. Technical Information Schöck Combar. Baden Baden: Schöck Bauteile GmbH, 2006. 23 p.

41. Gribniak V, Mang HA, Kupliauskas R, Kaklauskas G. Stochastic tension-stiffening approach for the solution of serviceability problems in reinforced concrete:

Constitutive modeling. Computer-Aided Civil and Infrastructure Engineering 2015;30(9):684-702.

42. Gribniak V, Rimkus A. Equipment for fastening group of reinforcement bars within structural concrete element. Patent No. LT 6275 B. Vilnius: State Patent Bureau of the Republic of Lithuania, 2016. 9 p. (in Lithuanian).

43. Rimkus A. Effects of Bar Reinforcement Arrangement on Deformations and Cracking of Concrete Elements. Doctoral Dissertation. Vilnius: Technika, 2017. 143 p.

44. Kaklauskas G, Gribniak V, Bacinskas D. Discussion of “Tension stiffening in lightly reinforced concrete slabs” by R. I. Gilbert. ASCE Journal of Structural Engineering 2008;134(7):1261-1262.

45. Gribniak V, Jakubovskis R, Rimkus A, Ng P-L, Hui D. Experimental and numerical analysis of strain gradient in tensile concrete prisms reinforced with multiple bars. Construction and Building Materials, in press.

Table 1. Relevant tensile properties of steel (experimental tests) and GFRP bars (from the supplier).

Material	∅, mm	E_r, GPa	Yielding		End of plastic stage		Ultimate load	
			ε_y	σ_y, MPa	ε_p	σ_p, MPa	ε_u	σ_u, MPa
Steel	6	205.9	0.0023	500.4	0.0035	577.7	0.0193	616.7
Steel	8	201.8	0.0025	520.3	0.0050	580.75	0.0391	626.0
Steel	10	191.7	0.0030	580.3	0.0242	620.1	0.0791	676.9
GFRP	8	63.5	–	–	–	–	0.0236	1500.0
GFRP	12	63.5	–	–	–	–	0.0213	1350.0

Table 2. Characteristics of the reinforcement configurations adopted in the experimental program.

Tie	GFRP reinforcement			Steel reinforcement			$\rho_{s,eq}$, %	$k_{f/s}^{a}$	p_f/p_s
	∅, mm	A_f , mm^2	E_f, GPa	∅, mm	A_s, mm^2	E_s, GPa			
4G12/4S10-1	12	452.4	63.5	10	314.2	194.6	2.05	0.47	1.2
4G12/4S10-2	12	452.4	63.5	10	314.2	194.6	2.05	0.47	1.2
4G12/4S6-1	12	452.4	63.5	6	113.1	203.6	1.13	1.25	2
4G12/4S6-2	12	452.4	63.5	6	113.1	203.6	1.13	1.25	2
4G8/4S8-1	8	201.1	63.5	8	201.1	197.1	1.18	0.32	1
4G8/4S8-2	8	201.1	63.5	8	201.1	197.1	1.18	0.32	1
4G8/4S6-1	8	201.1	63.5	6	113.1	203.6	0.78	0.55	1.3
4G8/4S6-2	8	201.1	63.5	6	113.1	203.6	0.78	0.55	1.3
8S10X	–	–	–	10	628.3	194.6	2.78	–	–
8S10R-1	–	–	–	10	628.3	194.6	2.78	–	–
8S10R-2	–	–	–	10	628.3	194.6	2.78	–	–

Table 3. Concrete compressive strength in cylinder specimens.

Cylinder	Age, days	Strength f_c, MPa	Average strength f_{cm}, MPa	CoV, %
C1	7	40.57	40.9	1.0
C2	7	41.30		
C3	7	40.74		
C4	14	44.39	44.4	1.5
C5	14	45.11		
C6	14	43.81		
C7	21	44.43	46.4	3.7
C8	21	47.55		
C9	21	47.15		
C10	28	50.68	49.3	2.5
C11	28	48.80		
C12	28	48.30		

Table 4. Cracking analysis results.

Average strain		Average crack spacing $\overline{L}_{cr}{}^{*}$, mm	Average crack width, mm			
Reinf. ε_r	Concrete surface ε_c		Calculated by Eq. (4a) with the reference to $\varepsilon_r{}^{\dagger}$	Calculated by Eq. (4a) with the reference to ε_c	Experimental (microscope)	Experimental (*DIC*)
4G12/4S6-1						
0.00169	0.00116	99.77	0.1580 (0.103)	0.1048	0.1188	0.1194
0.00224	0.00152	99.77	0.2132 (0.139)	0.1410	0.1563	0.1545
0.00420	0.00286	99.7	0.4080 (0.265)	0.2746	0.3075	0.2388
4G12/4S6-2						
0.00098	0.00081	194.52	0.1697 (0.110)	0.1356	0.0650	**0.1351**
0.00158	0.00143	97.26	0.1432 (0.093)	0.1281	0.0890	0.1657
0.00211	0.00187	97.26	0.1945 (0.126)	0.1715	0.1380	0.2336
0.00400	0.00350	77.81	0.3030 (0.197)	0.2640	0.2142	0.2646
4G12/4S10-1						
0.00070	0.00033	112.09	0.0657 (0.043)	0.0248	0.0775	0.0758
0.00130	0.00077	123.02	0.1469 (0.095)	0.0810	0.1067	0.1344
0.00186	0.00115	100.15	0.1751 (0.114)	0.1040	0.1583	**0.1462**
0.00243	0.00154	75.11	0.1746 (0.113)	0.1076	0.1513	**0.1292**
4G12/4S10-2						
0.00073	0.00037	182.60	0.1141 (0.074)	0.0480	0.0775	[0.1784]
0.00138	0.00076	91.30	0.1158 (0.075)	0.0595	0.1400	**0.1434**
0.00196	0.00118	80.68	0.1495 (0.097)	0.0861	0.1300	**0.1421**
0.00259	0.00163	81.21	0.2012 (0.131)	0.1232	0.1280	[0.1570]
4G8/4S8-1						
0.00107	0.00034	66.12	0.0634 (0.041)	0.0154	0.1050	[0.0372]
0.00186	0.00106	66.17	0.1158 (0.075)	0.0627	0.1010	**0.0986**
0.00278	0.00176	66.17	0.1766 (0.115)	0.1096	0.1520	**0.1255**
0.00688	0.00479	66.17	0.4480 (0.291)	0.3096	0.3658	[0.1880]
4G8/4S8-2						
0.00110	0.00043	84.99	0.0839 (0.055)	0.0270	0.1025	[0.0695]
0.00196	0.00099	91.64	0.1695 (0.110)	0.0807	0.1238	0.1709
0.00293	0.00162	91.64	0.2585 (0.168)	0.1385	0.1600	0.1957
0.00715	0.00504	92.90	0.6541 (0.425)	0.4579	0.4070	0.2776
4G8/4S6-1						
0.00199	0.00116	111.32	0.2093 (0.136)	0.1165	0.1867	0.1606
0.00681	0.00466	73.02	0.4894 (0.318)	0.3325	0.3633	[0.1876]
4G8/4S6-2						
0.00213	0.00111	125.93	0.2547 (0.166)	0.1263	0.1733	0.1587
0.00692	0.00396	83.95	0.5718 (0.372)	0.3235	0.5050	[0.1732]

*Average crack spacing obtained excluding external blocks of the concrete

†The calculated values in brackets improved by using the reduction coefficient α_{ε} from Eq. (6)

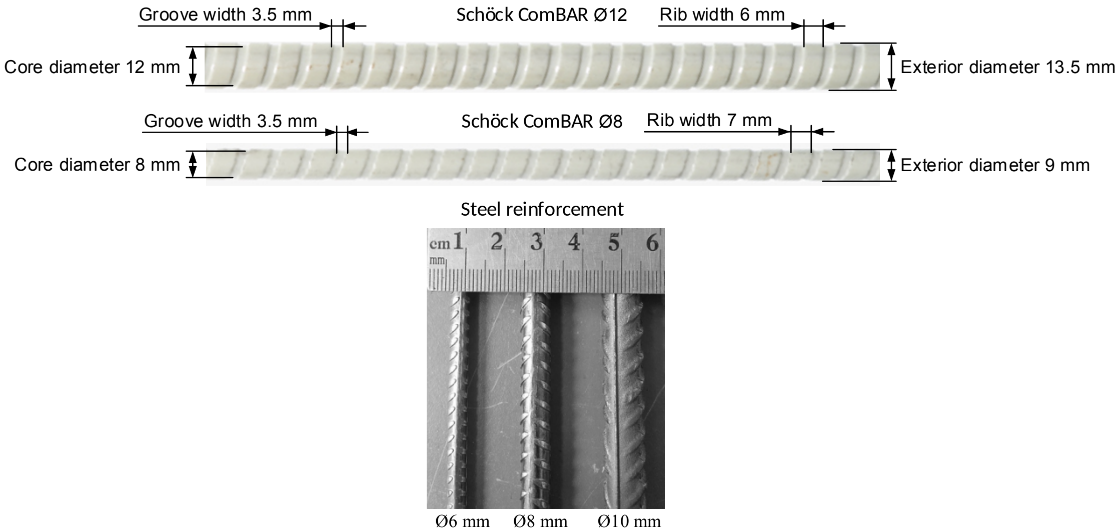

Fig. 1. Geometric characteristics of the GFRP and steel bars adopted in the ties.

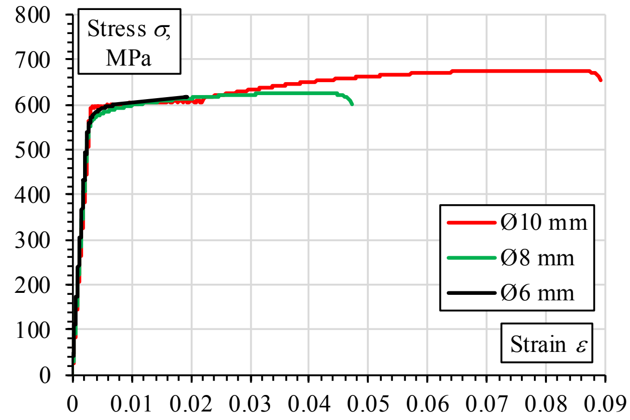

Fig. 2. Stress-strain curves from tensile tests with steel bars.

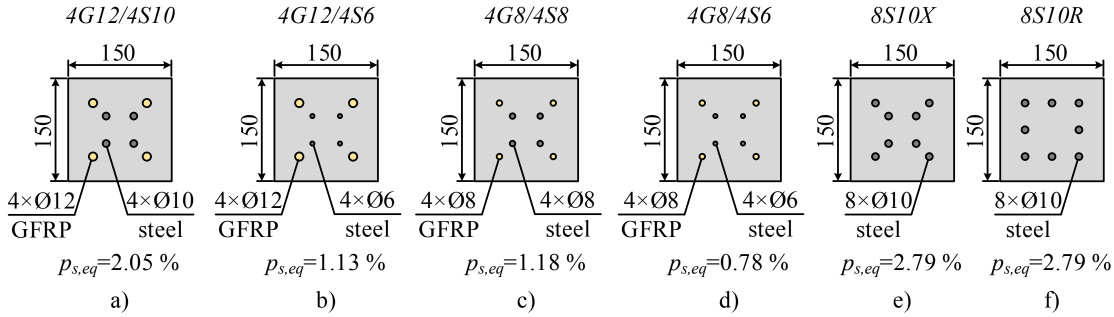

Fig. 3. Configurations of the reinforcement arrangements of the experimental program (concrete cover thickness: 30 mm of GFRP bars; 50 mm of steel bars).

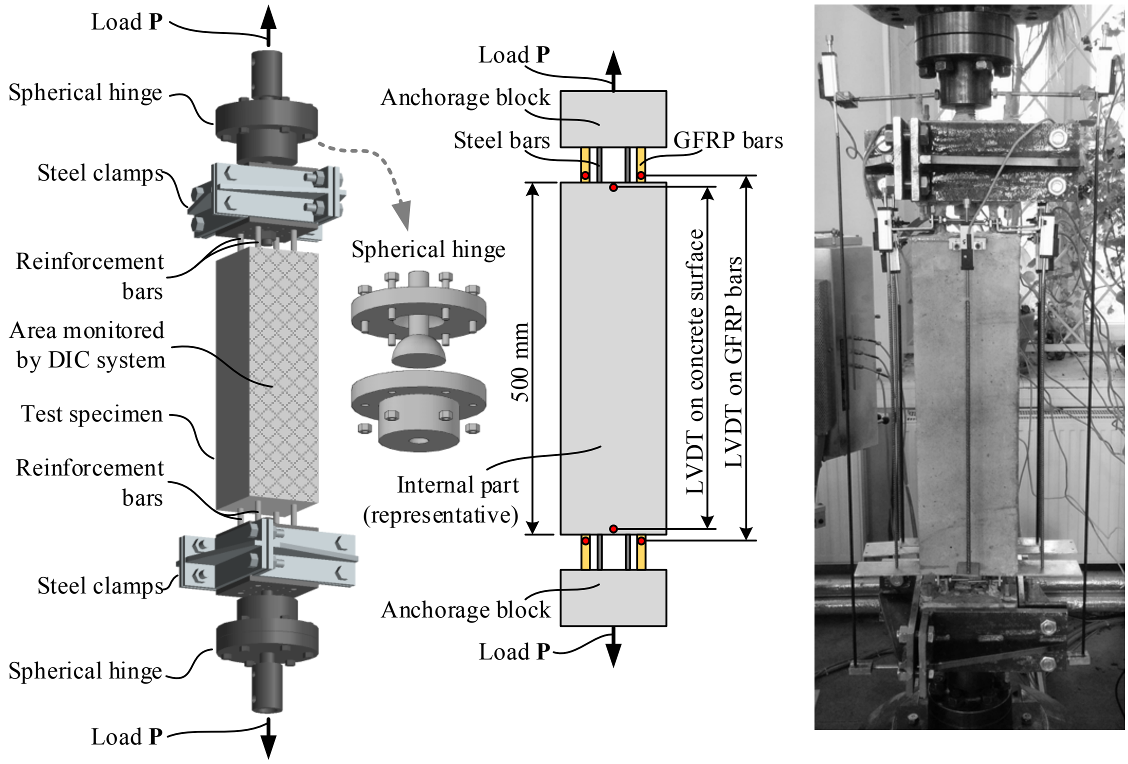

Fig. 4. Setup of the direct tensile tests.

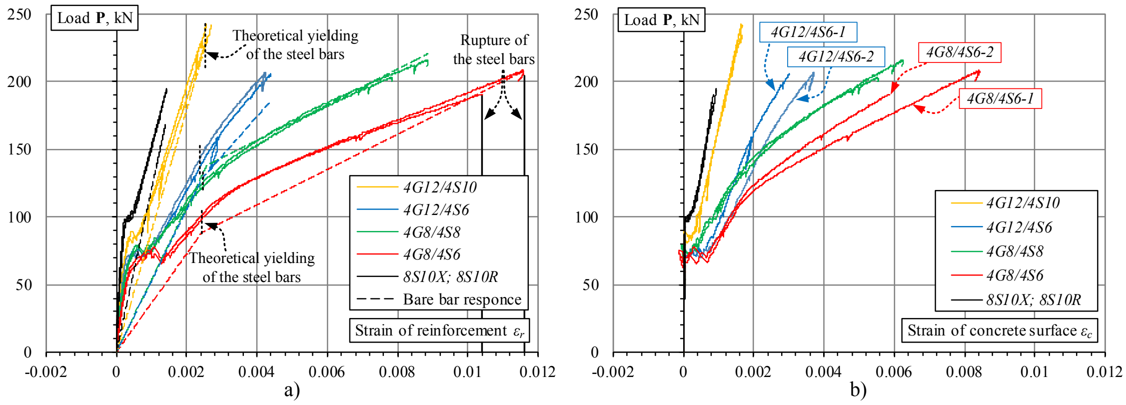

Fig. 5. Load-average strain diagrams determined using data of LVDT attached to: a) GFRP bars; b) concrete surface.

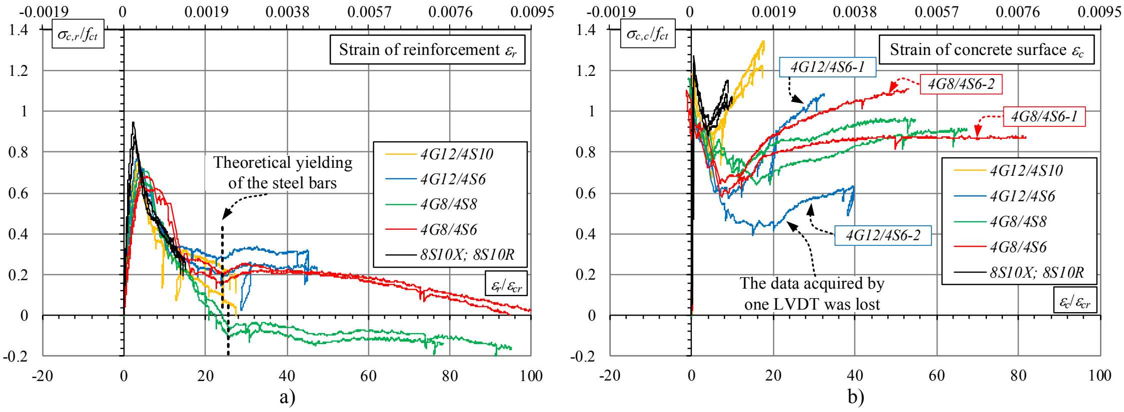

Fig. 6. Normalized average stress (divided by the theoretical tensile strength of the concrete) versus normalized average strain (divided by the theoretical cracking strain of the concrete) of: a) reinforcement; b) concrete surface.

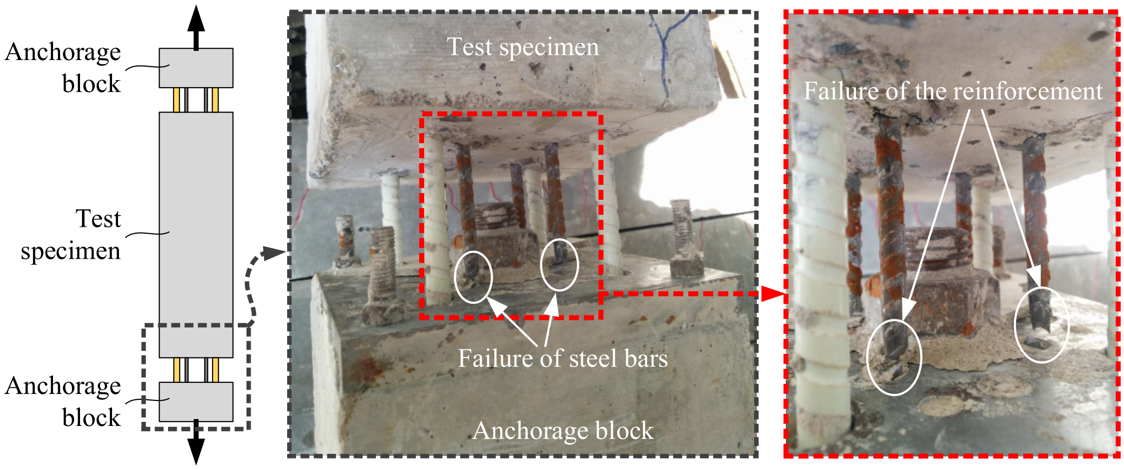

Fig. 7. Tensile rupture of the steel bars of the *4G8/4S6* ties in their uncovered extremities.

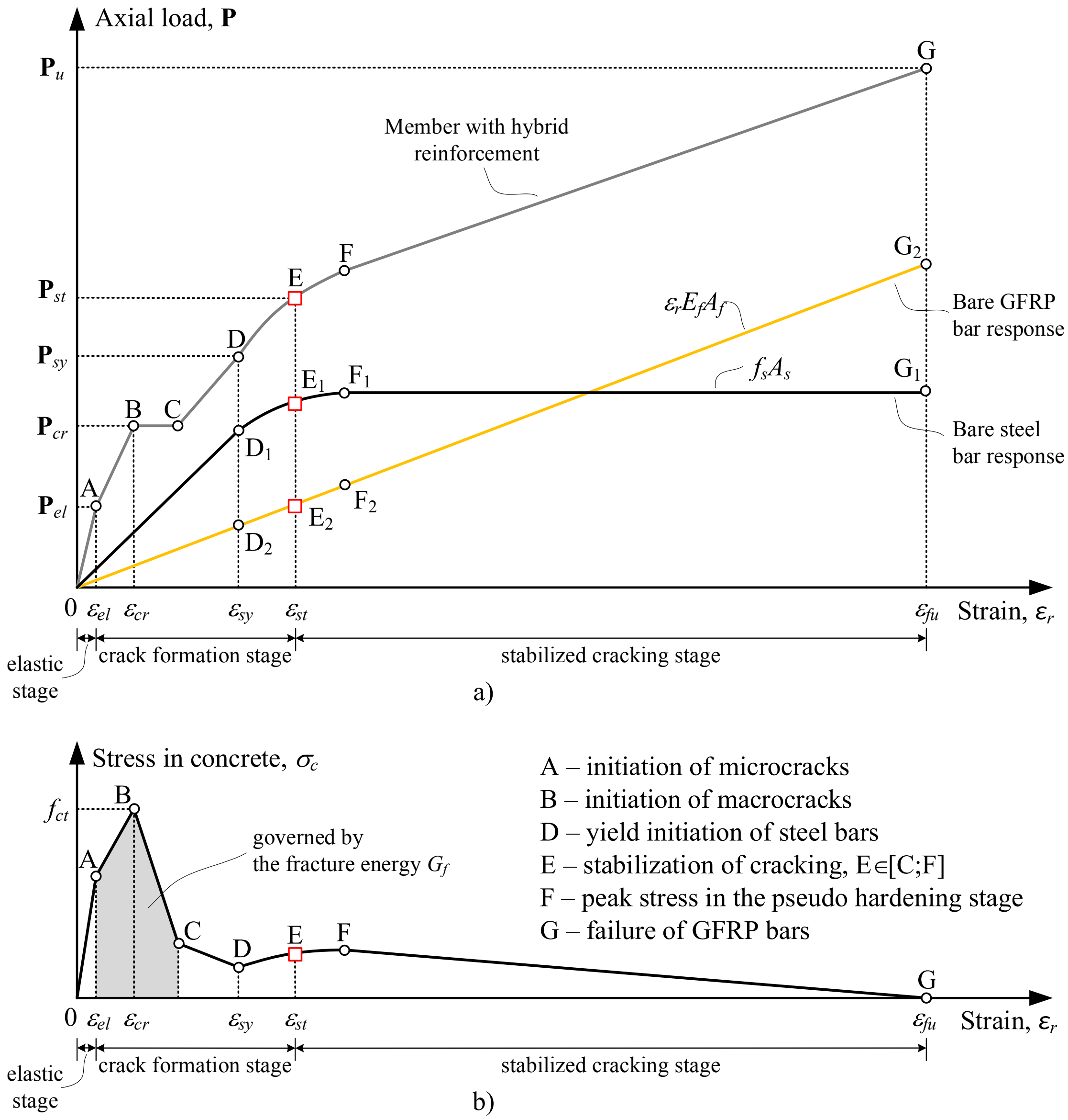

758

759 **Fig. 8.** Physical representation of the tension stiffening diagrams in concrete prisms

760 with hybrid reinforcement.

761

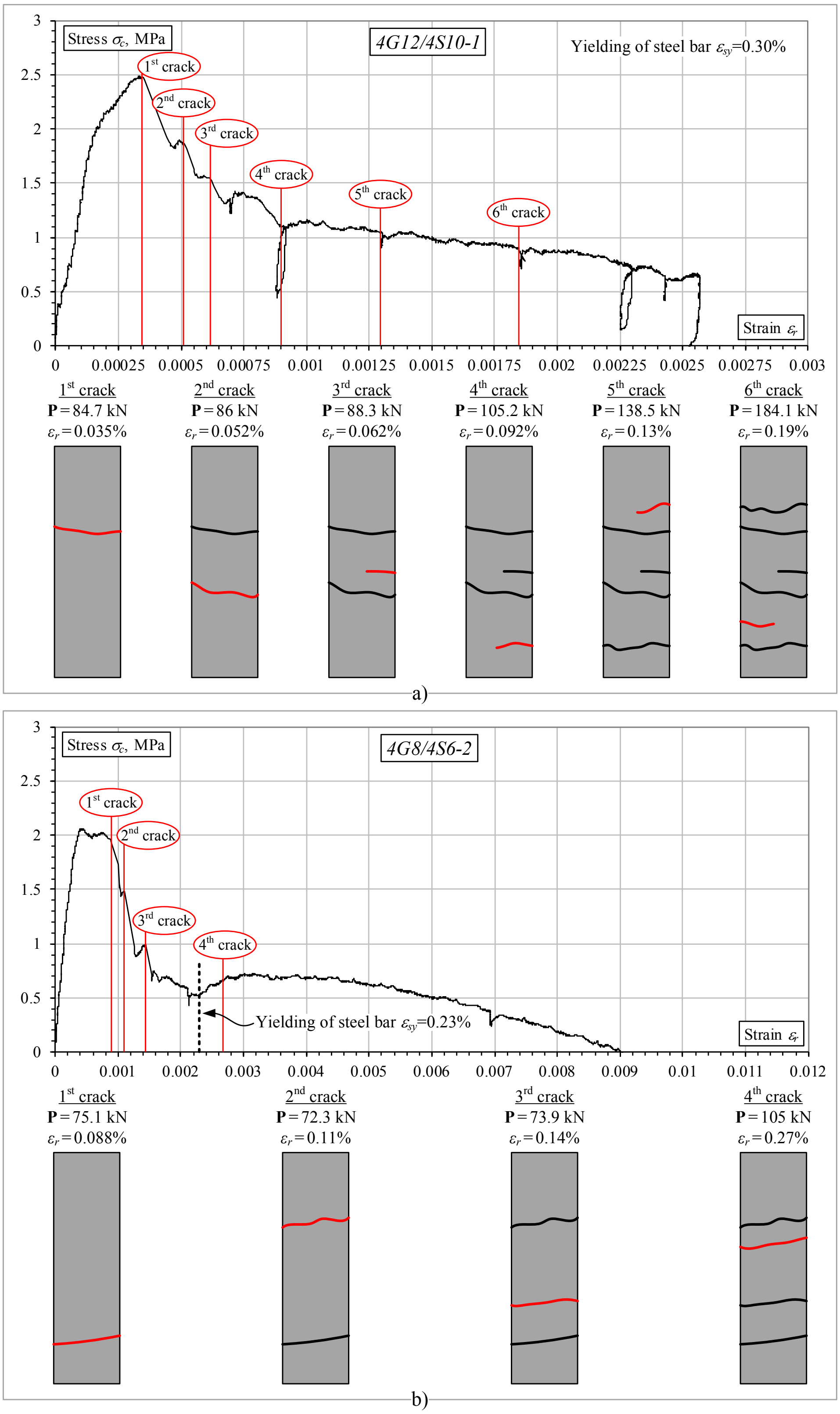

Fig. 9. Cracking process versus tension stiffening in the selected specimens: a) *4G12/4S10-1*; b) *4G8/4S6-2*.

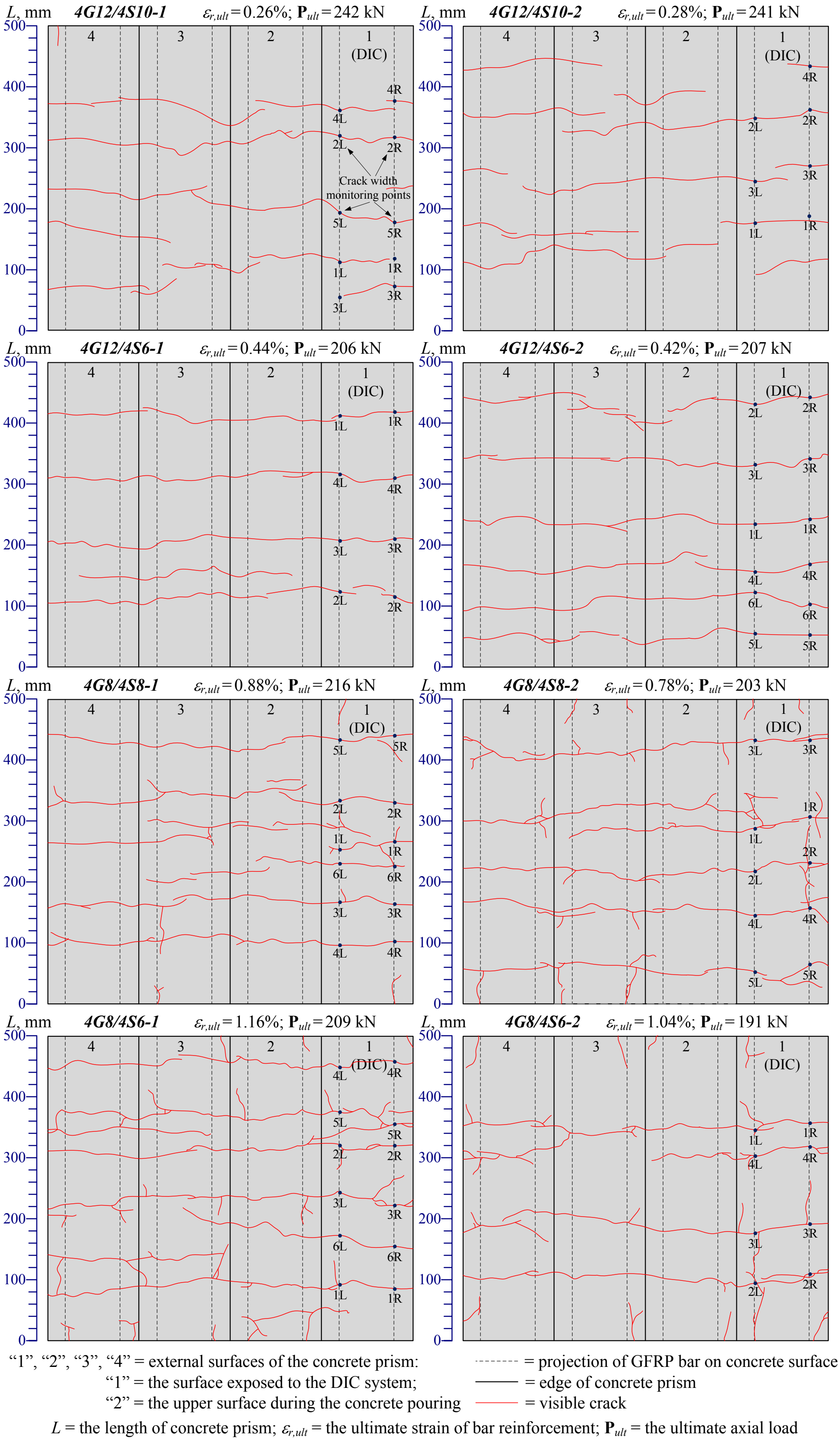

Fig. 10. Final crack patterns of the ties with hybrid reinforcement.

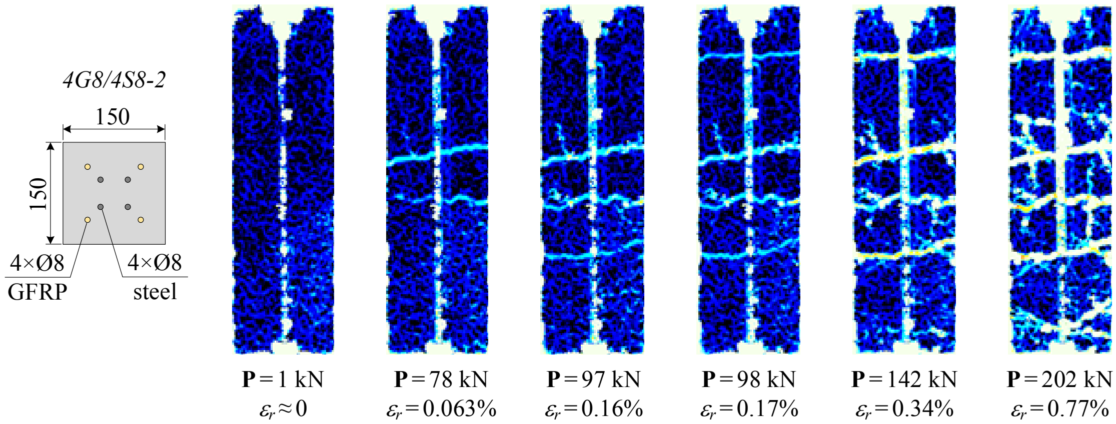

Fig. 11. DIC applied for the assessment of the cracking process in *4G8/4S8-2* sample.

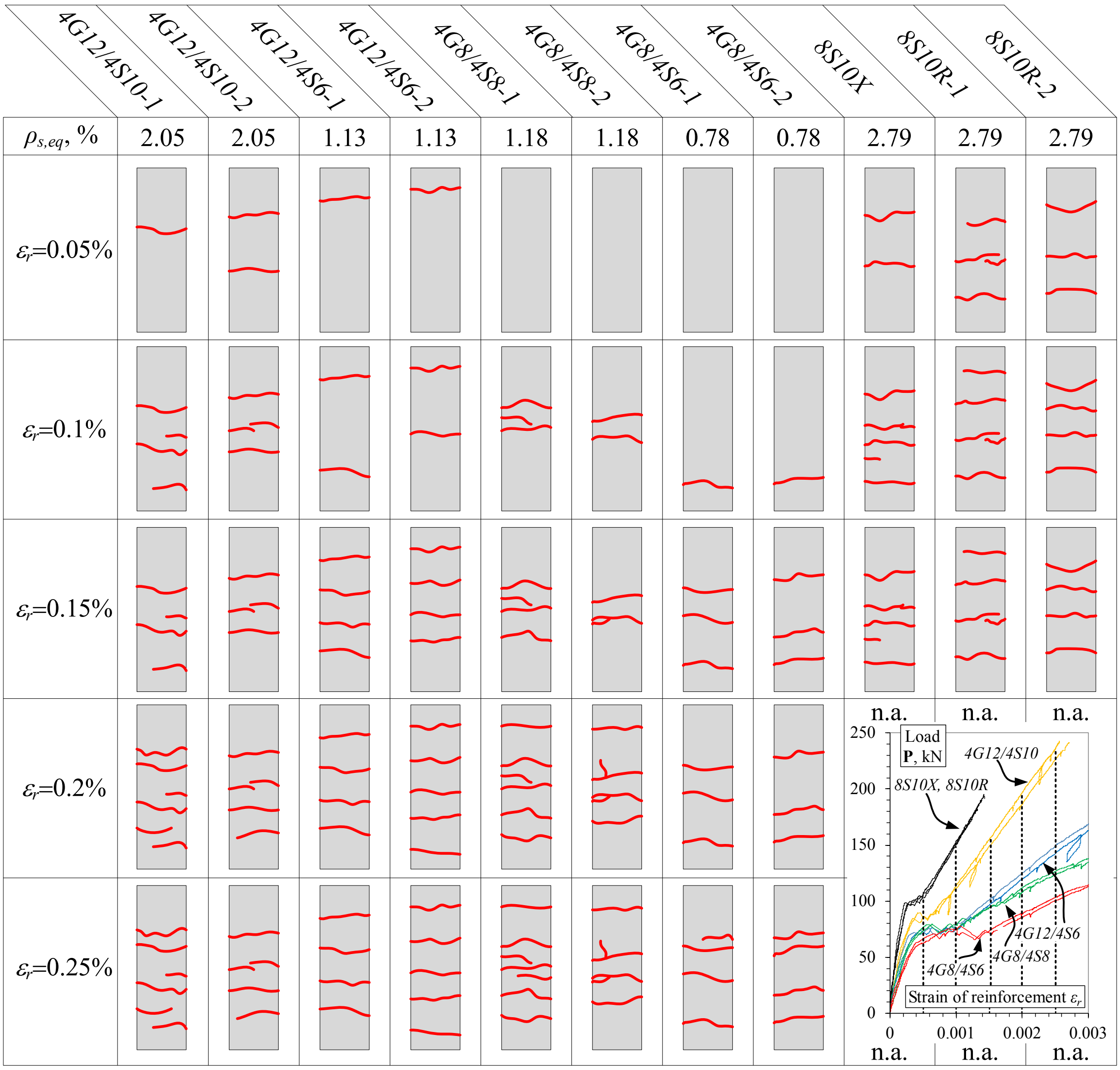

Fig. 12. Crack patterns of all ties identified using the DIC system.

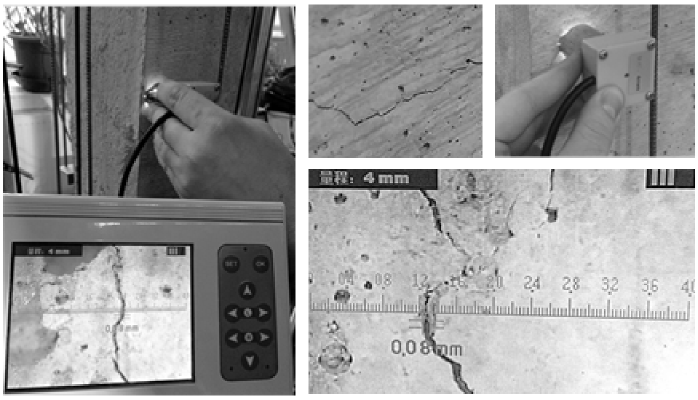

Fig. 13. Crack measurement using digital microscope *CK102* (with 40× magnification).

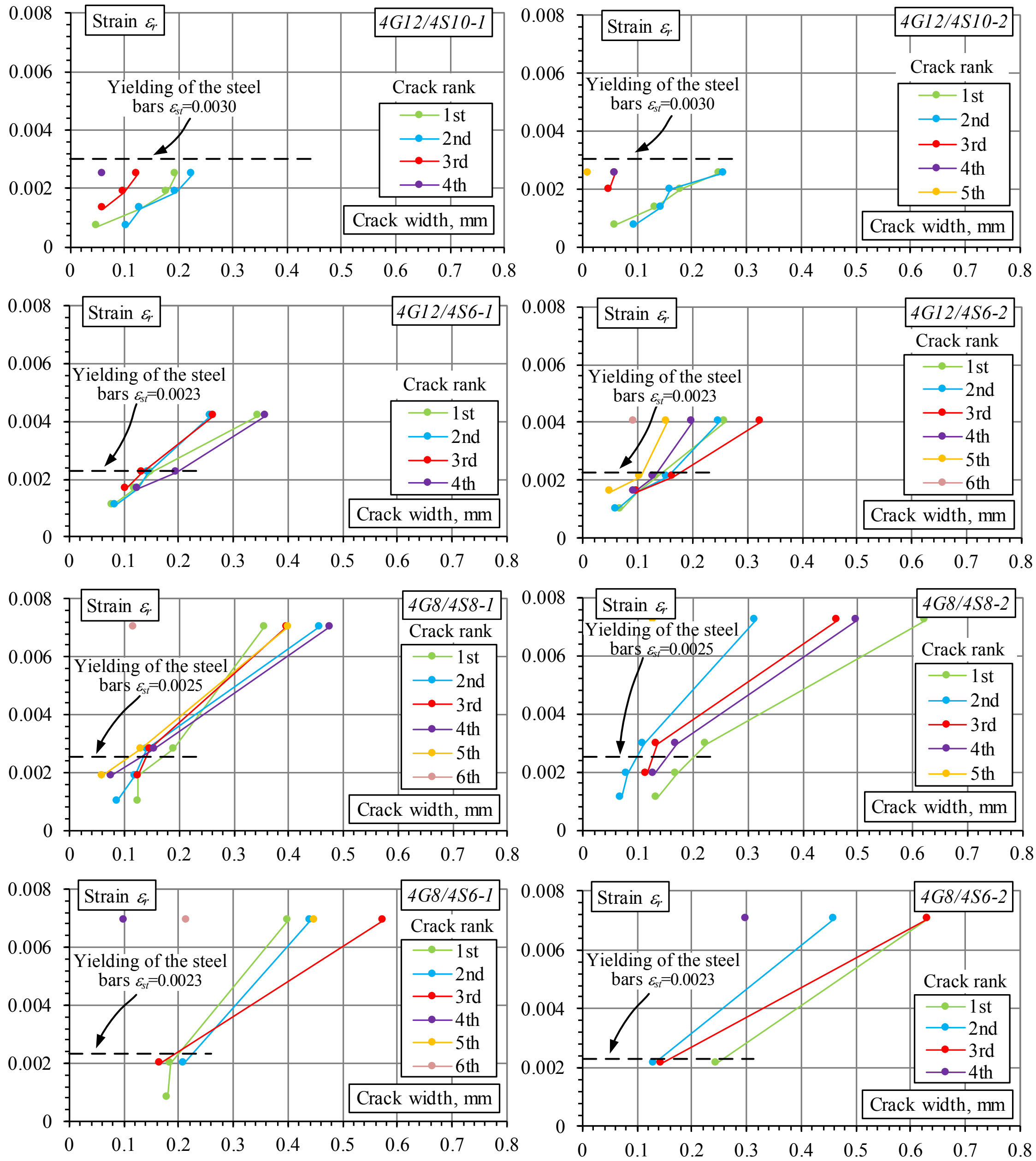

Fig. 14. Crack evolution in the ties with hybrid reinforcement (numbers indicate cracking sequence).

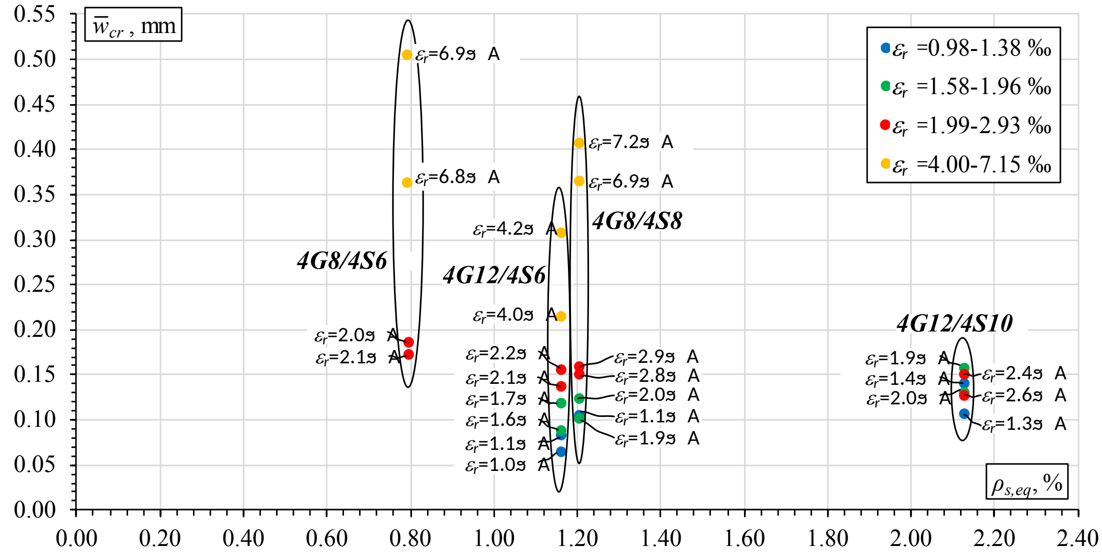

Fig. 15. Relationship between equivalent steel reinforcement ratio, $\rho_{s,eq}$, and average crack width obtained using the optical microscope.

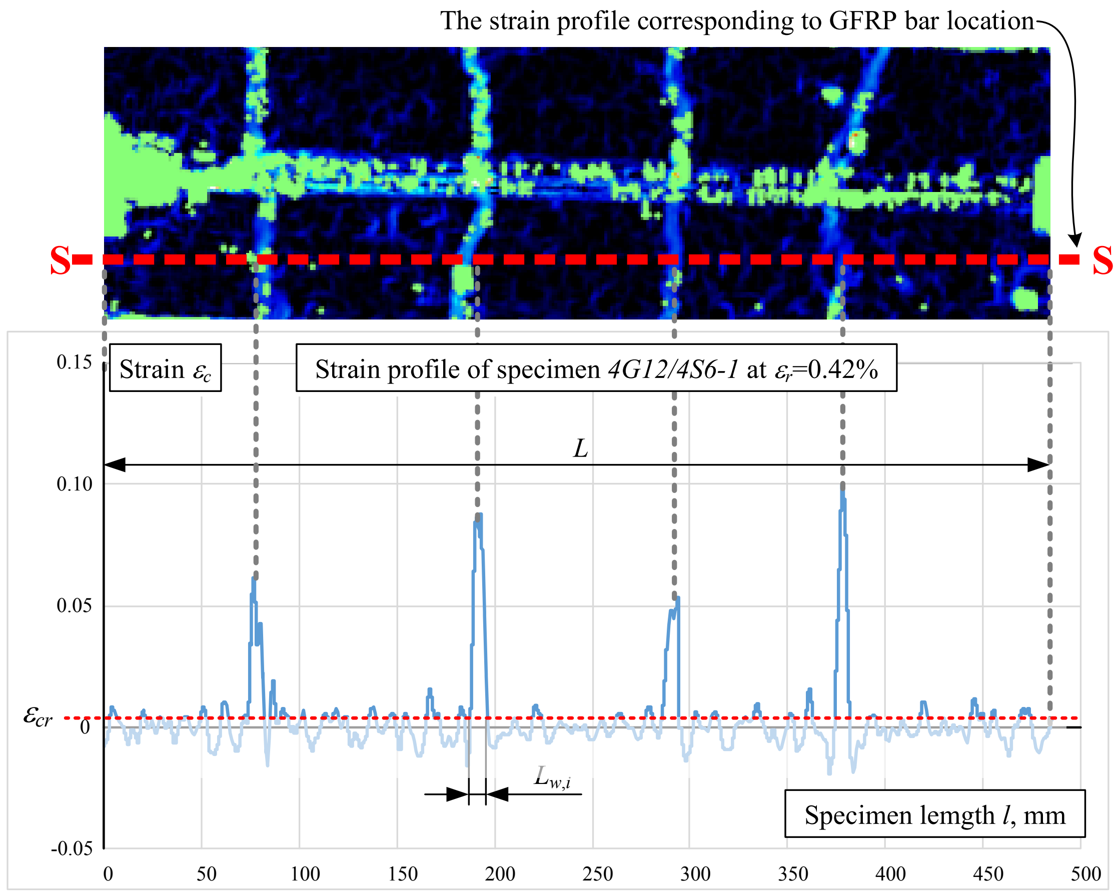

Fig. 16. A schematic illustration of the crack estimation using the DIC results.

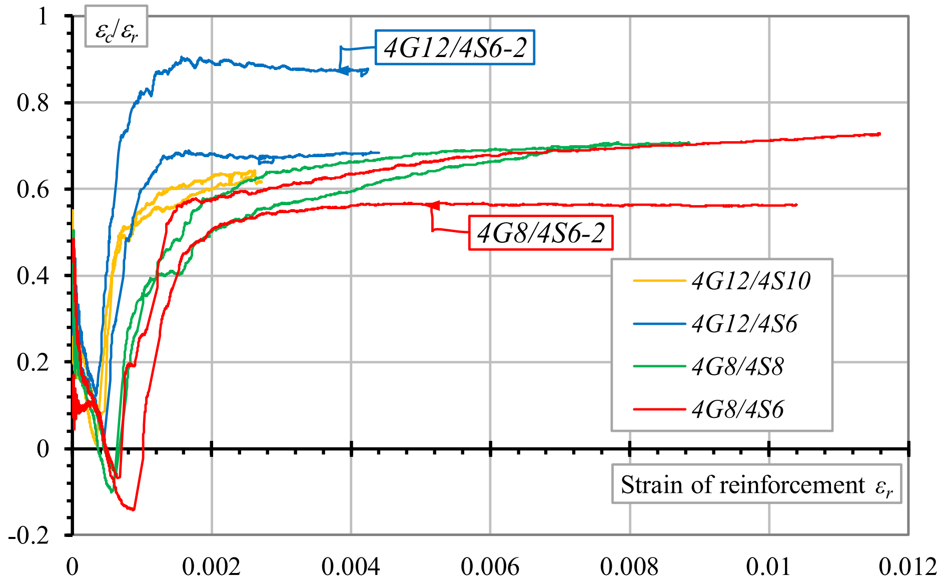

Fig. 17. Evolution of the average concrete and reinforcement strain ratio, $\varepsilon_c/\varepsilon_r$, with increasing deformations of the reinforcement.

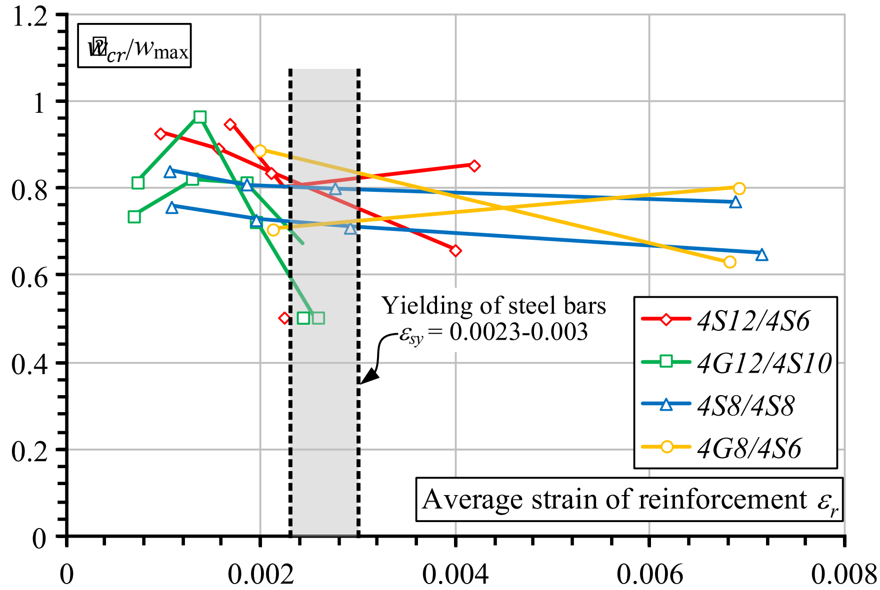

791

792 **Fig. 18.** Relationship between average strain of reinforcement and average and

793 maximal crack width (obtained using the optical microscope) ratio.